DOI: 10.48011/asba.v2i1.1616

Robust optimal nonlinear control strategies for an aerial manipulator ⋆

Júnio E. de Morais * **Daniel Neri** * **Guilherme V. Raffo** *,**

* *Graduate Program in Electrical Engineering, Federal University of Minas Gerais, MG, (e-mail: {jeduardo, danielneri}@ufmg.br).*
** *Department of Electronic Engineering, Federal University of Minas Gerais, MG (e-mail: raffo@ufmg.br)*

Abstract: This work presents two control strategies based on a classic nonlinear $\mathscr{H}_\infty$ controller and on a novel nonlinear $\mathscr{W}_\infty$ controller for robust trajectory tracking of an unmanned aerial manipulator (UAM). The controllers are implemented in a hardware-in-the-loop (HIL) framework using the ProVANT simulator, which was developed on the Gazebo and Robot Operating System (ROS) platforms. In addition, the performance of these controllers is compared in order to highlight their advantages and disadvantages.

Keywords: Unmanned aerial manipulator, Lagrangian systems, Robust control, Nonlinear control, Sobolev space.

1. INTRODUCTION

Unmanned aerial manipulators (UAMs) consist of unmanned aerial vehicles (UAVs) coupled with one or more robotic manipulators. These aerial robots expand the workspace of a robotic manipulator to encompass all of the accessible (i.e. obstacle-free) tridimensional space, presenting a vast potential in the realization of tasks in remote, hard to access, and hazardous environments. Despite the advantages, developing UAMs is not a trivial task. These systems are usually underactuated mechanical systems with highly coupled and complex nonlinear dynamics. In addition, the UAMs operate under the effects of disturbances caused by aerodynamic effects, unmodeled dynamics and parametric uncertainties, as well as those effects related to the displacements of the center of mass generated by the movements of the robotic arm. Therefore, this kind of systems require robust controllers in order to achieve acceptable performance.

In the literature, few works deal with control design for UAMs. In Mello et al. (2015), feedback linearization with PD controller was designed for a UAM. In Lippiello and Ruggiero (2012), a cartesian impedance control law was proposed, while Johansen et al. (2019) used a PD+ controller based on dual quaternions. Acosta et al. (2014) proposed a robust passivity based controller that ensures stability with the robotic arm locked at any position. In Heredia et al. (2014), a backstepping based controller for the UAV and admittance controller for the robotic arm were implemented; while in Jimenez-Cano et al. (2013), the same backstepping based controller was used for the UAV, but with a PID based controller for the robotic arm. In Ballesteros-Escamilla et al. (2019), an adaptive controller based on a PD structure was proposed for the trajectory tracking of an UAM. In Acosta et al. (2020) a nonlinear cascade control strategy is presented, with a passivity based controller for the UAV and an inverse kinematic controller with integral action for the robotic manipulator. And Nava et al. (2020) present a controller based on multi-task optimization for an UAM equipped with a force sensor in its end effector.

Among the fundamental nonlinear control strategies used to handle and attenuate disturbances, the classic $\mathscr{H}_\infty$ control theory is one of the most used. This control strategy aims to achieve a small and bounded ratio between the external disturbances and the cost variable (van der Schaft, 2000). Some applications of nonlinear $\mathscr{H}_\infty$ controllers to underactuated mechanical systems are found in Siqueira and Terra (2004b); Raffo et al. (2011, 2015). The efficiency of the nonlinear $\mathscr{H}_\infty$ controller has already been demonstrated through several experiments. Nevertheless, this control approach presents some drawbacks. As stated in Chilali and Gahinet (1996), the $\mathscr{H}_\infty$ control strategy deals mostly with the aspect of the highest gain that the system gives to the disturbances, and provides little control over the transient behavior of the system. To overcome this issue, Aliyu and Boukas (2011) proposed the formulation of the $\mathscr{H}_\infty$ controller in the Sobolev space $\mathscr{W}_{m,p}$ for the general class of nonlinear systems. Later, Neri et al. (2018) particularized this approach for mechanical systems and extended it to the weighted Sobolev space. The reasoning behind this new control approach is to consider the dynamics of the system in the cost functional in order to obtain a controller that provides better transient response with fast reaction against external disturbances. These features make the $\mathscr{W}_\infty$ controller more attractive for the control design of UAMs than the classic $\mathscr{H}_\infty$ control strategy.

⋆ This work was in part supported by the project INCT (National Institute of Science and Technology) under the grant CNPq (Brazilian National Research Council) 465755/2014-3, FAPESP (São Paulo Research Foundation), Brazil 2014/50851-0. This work was also supported in part by the Coordenação de Aperfeiçoamento de Pessoal de Nível Superior (CAPES), Brazil (Finance Code 88887.136349/2017-00, and 001), CNPq, Brazil (grant numbers 313568/2017-0 and 426392/2016-7), and FAPEMIG, Brazil (grant number APQ-03090-17).

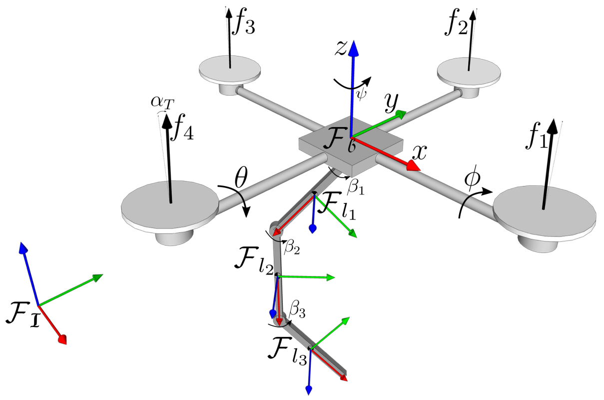

Figure 1. Reference frames rigid attached to the mechanical system in order to derive the forward kinematic.

Therefore, aiming to achieve a robust trajectory tracking, this paper presents two control strategies based on the classic nonlinear $\mathscr{H}_\infty$ controller and on the novel nonlinear $\mathscr{W}_\infty$ controller for a UAM. Numerical experiments are conducted in a hardware-in-the-loop (HIL) framework using the ProVANT simulator, which was developed on the Gazebo and Robot Operating System (ROS) platforms using the Computer-Aided Design (CAD) model of the UAM. In order to assess the performance of the designed controllers, a quantitative comparative analysis is performed based on the Integral Square Error (ISE) and the Integral of Absolute value of the control Derivative (IADu) indexes.

Summarizing, the main contributions of this paper are: (i) the design of two robust control strategies for trajectory tracking of an unmanned aerial manipulator based on the nonlinear $\mathscr{H}_\infty$ controller, proposed in Raffo et al. (2011), and on the novel nonlinear $\mathscr{W}_\infty$ controller, proposed in Neri et al. (2018), followed by a comparative analysis between their performances; and (ii) the implementation of these controllers in a HIL framework using the high fidelity ProVANT Simulator [1] . Accordingly, the remaining of the paper is structured as: Section 2 describes the modeling of the UAM; Section 3 presents the nonlinear $\mathscr{H}_\infty$ and $\mathscr{W}_\infty$ control approaches designed for underactuated mechanical systems; Section 4 illustrates the numerical experiments and presents the comparative analysis. Finally, Section 5 concludes the work and presents future works.

2. SYSTEM MODELING

The UAM presented in this work consists of a quadrotor UAV serially coupled with a planar manipulator composed of three revolute joints (see Figure 1). To obtain the forward kinematics, five frames are rigid attached to the system, they are shown in Figure 1 and are defined as: $\mathcal{F}_{\mathbf{I}}$ is the inertial frame, $\mathcal{F}_{\mathit{6}}$ is a frame attached to the center of mass of the UAV, and $\mathcal{F}_{l_i}$ is attached to the center of mass of the *i-th* link of the manipulator, with $i \in \{1,\ 2,\ 3\}$.

The quadrotor UAV has six degrees of freedom (DOF) $\mathbf{q}_q \triangleq [\phi\ \theta\ \psi\ x\ y\ z]'$, where x, y, and z denote the position of the origin of $\mathcal{F}_{\mathit{6}}$ with respect to (w.r.t.) $\mathcal{F}_{\mathbf{I}}$, and ϕ, θ, and ψ are Euler angles that describe the orientation of $\mathcal{F}_{\mathit{6}}$ w.r.t. $\mathcal{F}_{\mathbf{I}}$ using the roll, pitch and yaw convention. The manipulator arm has three degrees of freedom $\mathbf{q}_m \triangleq [\beta_1\ \beta_2\ \beta_3]'$, where β_i is the angular position of the i-th joint w.r.t the (i-1)-th joint. Thus, the complete system possesses nine DOF, with the vector of generalized coordinates given by $\mathbf{q} \triangleq \left[\mathbf{q}_q'\ \mathbf{q}_m'\right]'$.

Initially, the forward kinematics are developed. Therefore, the pose of the quadrotor UAV w.r.t. $\mathcal{F}_{\mathbf{I}}$ are computed by means of the following homogeneous transformation matrix [2] :

$$\mathbf{H}_{\mathit{6}}^{\mathbf{I}} = \begin{bmatrix} \mathbf{R}_{\mathit{6}}^{\mathbf{I}} & \mathbf{p}_{\mathit{6}}^{\mathbf{I}} \\ \mathbf{0} & 1 \end{bmatrix}, \tag{1}$$

where $\mathbf{R}_{\mathit{6}}^{\mathbf{I}} \triangleq \mathbf{R}_{z,\psi}\mathbf{R}_{y,\theta}\mathbf{R}_{x,\phi} \in \mathrm{SO}(3)$ is the orthonormal rotation matrix, $\mathbf{p}_{\mathit{6}}^{\mathbf{I}} = [x\ y\ z]'$ is a vector that describes the position of the quadrotor UAV, and $\mathbf{0}$ is a matrix of zeros with appropriate dimension.

The pose of the center of mass of the manipulator links w.r.t. the UAV fixed frame are determined using the standard Denavit-Hartenberg (DH) convention (Spong et al., 2006), with the parameters a_i, α_i, d_i and ϑ_i presented in Table 1. Therefore, under the DH convention, the transformation matrix from the $i-th$ link to the previous $(i-1)-th$ link in the chain is given by

$$\mathbf{H}_{l_i}^{l_{i-1}} = \begin{bmatrix} \mathbf{R}_{l_i}^{l_{i-1}} & \mathbf{p}_{l_i}^{l_{i-1}} \\ \mathbf{0} & 1 \end{bmatrix}, \tag{2}$$

with

$$\mathbf{R}_{l_i}^{l_{i-1}} = \begin{bmatrix} \cos\vartheta_i & -\sin\vartheta_i\cos\alpha_i & \sin\vartheta_i\sin\alpha_i \\ \sin\vartheta_i & \cos\vartheta_i\cos\alpha_i & -\cos\vartheta_i\sin\alpha_i \\ 0 & \sin\alpha_i & \cos\alpha_i \end{bmatrix}, \tag{3}$$

$$\mathbf{p}_{l_i}^{l_{i-1}} = \begin{bmatrix} a_i\cos\vartheta_i \\ a_i\sin\vartheta_i \\ d_i \end{bmatrix}. \tag{4}$$

In this way, the homogeneous transformation matrix from the *i-th* link to inertial frame is computed by

$$\mathbf{H}_{l_i}^{\mathbf{I}} = \begin{bmatrix} \mathbf{R}_{l_i}^{\mathbf{I}} & \mathbf{p}_{l_i}^{\mathbf{I}} \\ \mathbf{0} & 1 \end{bmatrix} = \mathbf{H}_{\mathit{6}}^{\mathbf{I}}\mathbf{H}_{l_0}^{\mathit{6}}\mathbf{H}_{l_1}^{l_0}\cdots\mathbf{H}_{l_i}^{l_{i-1}}. \tag{5}$$

2.1 *Equations of Motion*

The dynamic modeling of the system follows the methodology presented in Lippiello and Ruggiero (2012), making use of the Euler-Lagrange formalism. The resulting equations of motion are given in the canonical form as

$$\mathbf{M}(\mathbf{q})\ddot{\mathbf{q}} + \mathbf{C}(\mathbf{q},\dot{\mathbf{q}})\dot{\mathbf{q}} + \mathbf{G}(\mathbf{q}) = \mathbf{u} + \boldsymbol{\delta}(t) \tag{6}$$

where $\mathbf{M}(\mathbf{q}) \in \mathbb{R}^{9\times 9}$ is the symmetric and positive definite inertia matrix, $\mathbf{C}(\mathbf{q},\dot{\mathbf{q}}) \in \mathbb{R}^{9\times 9}$ is the centrifugal and Coriollis forces matrix, $\mathbf{G}(\mathbf{q}) \in \mathbb{R}^9$ is the vector of gravitational forces, $\mathbf{u} \in \mathbb{R}^9$ is the vector of generalized forces, and $\boldsymbol{\delta}(t) = [\delta_\phi\ \delta_\theta\ \delta_\psi\ \delta_x\ \delta_y\ \delta_z\ \delta_{\beta_1}\ \delta_{\beta_2}\ \delta_{\beta_3}]' \in \mathbb{R}^9$ is the vector of generalized disturbances that affect the system.

The inertia matrix is computed through the UAM total kinetic energy. Therefore, using the previous defined forward kinematics, the inertia matrix is given by

[1] The ProVANT simulator is an open source software developed for testing control strategies on UAVs. It is available to download on `https://github.com/Guiraffo/ProVANT-Simulator`.

[2] From now on, the frame notations $\mathcal{F}_{\mathbf{I}}$, $\mathcal{F}_{\mathit{6}}$ and $\mathcal{F}_{l_i}$ will be simplified to $\mathbf{I}$, $\mathit{6}$ and l_i, respectively

$$\mathbf{M}(\mathbf{q}) = \begin{bmatrix} \mathbf{M}_{11} & \mathbf{M}_{12} & \mathbf{M}_{13} \\ * & \mathbf{M}_{22} & \mathbf{M}_{23} \\ * & * & \mathbf{M}_{33} \end{bmatrix}, \tag{7}$$

in which the $*$ terms are deduced by the symmetry of $\mathbf{M}(\mathbf{q})$, and

$\mathbf{M}_{11} = \mathbf{W}_\eta' \mathcal{I}_q \mathbf{W}_\eta + \sum_{i=1}^{3} \left(m_{l_i} \mathcal{S}_{li}' \mathcal{S}_{li} + \mathbf{W}_\eta' \mathcal{J}_{li} \mathbf{W}_\eta \right),$

$\mathbf{M}_{12} = -\sum_{i=1}^{3} \left(m_{l_i} \mathcal{S}_{li} \right),\ \mathbf{M}_{13} = \sum_{i=1}^{3} \left(m_{l_i} \mathbf{R}_{\mathcal{b}}^{\mathcal{I}} \bar{\mathbf{J}}_v^{\,(l_i)} \right),$

$\mathbf{M}_{22} = \left(m_q + \sum_{i=1}^{3} m_{li} \right) \mathbb{1},\ \mathbf{M}_{23} = \sum_{i=1}^{3} \left(\mathbf{W}_\eta' \mathcal{J}_{li} \bar{\mathbf{J}}_\omega^{(l_i)} - m_{l_i} \mathcal{S}_{li} \mathbf{R}_{\mathcal{b}}^{\mathcal{I}} \bar{\mathbf{J}}_v^{(l_i)} \right),$

$\mathbf{M}_{33} = \sum_{i=1}^{3} m_{l_i} (\bar{\mathbf{J}}_v^{(l_i)})' \bar{\mathbf{J}}_v^{(l_i)} + (\bar{\mathbf{J}}_\omega^{l_i})' \mathcal{J}_{li} \bar{\mathbf{J}}_\omega^{l_i},$

with $\mathcal{S}_{li} = \mathbf{S}\left(\mathbf{R}_{\mathcal{b}}^{\mathcal{I}} \mathbf{p}_{l_i}^{\mathcal{b}}\right) \mathbf{W}_{\mathcal{I}}$, $\mathcal{J}_{li} = \mathbf{R}_{l_i}^{\mathcal{b}} \mathcal{I}_{l_i} (\mathbf{R}_{l_i}^{\mathcal{b}})'$, $\bar{\mathbf{J}}_v^{(li)} = \partial \mathbf{p}_{l_i}^{\mathcal{I}} / \partial \mathbf{q}$, $\bar{\mathbf{J}}_\omega^{(li)} = \partial \boldsymbol{\omega}_{l_i,\mathcal{b}}^{\mathcal{I}} / \partial \mathbf{q}$, $\mathbf{W}_{\mathcal{I}} = \mathbf{R}_{\mathcal{b}}^{\mathcal{I}} \mathbf{W}_\eta$, and

$$\mathbf{W}_\eta = \begin{bmatrix} 1 & 0 & -\sin\phi \\ 0 & \cos\phi & \sin\phi\cos\theta \\ 0 & -\sin\phi & \cos\phi\cos\theta \end{bmatrix}.$$

Moreover, $\mathbb{1}$ is an identity matrix with appropriate dimension, $\bar{\mathbf{J}}_v^{(li)} \in \mathbb{R}^{3\times 9}$ and $\bar{\mathbf{J}}_\omega^{(li)} \in \mathbb{R}^{3\times 9}$ are, respectively, the geometric Jacobian matrices of the linear and angular velocities of the *i-th* link, m_q and $\mathcal{I}_q$ are the mass and inertia tensor matrix of the quadrotor UAV, and m_{li} and $\mathcal{I}_{li}$ are the mass and inertia tensor matrix of the *i-th* link of the manipulator arm. Finally, $\mathbf{S}(\cdot)$ is a skew symmetric matrix (Spong et al., 2006) that satisfies $\mathbf{S}(\cdot)\,\mathbf{v} = \cdot \times \mathbf{v}$ for any vector $\mathbf{v} \in \mathbb{R}^3$, and the link angular velocity, $\boldsymbol{\omega}_{l_i}^{\mathcal{I}} \in \mathbb{R}^3$, is obtained from $\dot{\mathbf{R}}_{l_i}^{\mathcal{I}} \mathbf{R}_{l_i}^{\mathcal{I}} = \mathbf{S}(\boldsymbol{\omega}_{l_i,\mathcal{b}}^{\mathcal{I}})$.

From the inertia matrix, one can compute the Coriolis matrix, $\mathbf{C}(\mathbf{q}, \dot{\mathbf{q}})$, using the Christoffel symbols of the first kind as follows

$$\mathbf{C}_{ij} = \sum_{k=1}^{9} \frac{1}{2} \left(\frac{\partial \mathbf{M}_{ij}}{\partial \mathbf{q}_k} + \frac{\partial \mathbf{M}_{ik}}{\partial \mathbf{q}_j} - \frac{\partial \mathbf{M}_{jk}}{\partial \mathbf{q}_i} \right) \dot{\mathbf{q}}_k, \tag{8}$$

where $\mathbf{C}_{k,j}$ and $\mathbf{M}_{k,j}$ are elements of the Coriolis and inertia matrices, respectively, corresponding to the k-th row and j-th column.

In addition, the potential energy of this system is computed by

$$\mathcal{U} = -g \left[m_q \mathbf{e}_3' + \sum_{i=1}^{3} m_{l_i} \mathbf{e}_3' (\mathbf{p}_{\mathcal{b}}^{\mathcal{I}} + \mathbf{R}_{\mathcal{b}}^{\mathcal{I}} \mathbf{p}_{l_i}^{\mathcal{b}}) \right], \tag{9}$$

where $\mathbf{e}_3 = [0\ 0\ 1]'$, and g is the acceleration of gravity. Therefore, the gravitational force vector is given by $\mathbf{G}(\mathbf{q}) = \partial \mathcal{U} / \partial \mathbf{q}$.

Finally, the vector of generalized forces is computed by $\mathbf{u} = \mathbf{B}(\mathbf{q})\boldsymbol{\Gamma}$, in which $\boldsymbol{\Gamma} = [f_1\ f_2\ f_3\ f_4\ \tau_1\ \tau_2\ \tau_3]' \in \mathbb{R}^{n_c}$ is the vector of control inputs with f_n being the force applied by the *n-th* propeller, for $n \in \{1,\ 2,\ 3,\ 4\}$, τ_i the torque applied to the *i-th* joint of the manipulator arm, and $\mathbf{B}(\mathbf{q}) \in \mathbb{R}^{9\times 7}$ the input coupling matrix. To improve the controllability of the system, the rotors of the quadrotor UAV are tilted towards its geometric center by a small angle α_T (Raffo et al., 2011). Then, the input coupling matrix of the system is given by

$$\mathbf{B}(\mathbf{q}) = \begin{bmatrix} \mathbf{N}(\mathbf{q}) & \mathbf{0}_{6\times 3} \\ \mathbf{0}_{3\times 4} & \mathbb{1}_{3\times 3} \end{bmatrix}, \mathbf{N}(\mathbf{q}) = \begin{bmatrix} \mathbf{W}_\eta' & \mathbf{0}_{3\times 3} \\ \mathbf{0}_{3\times 3} & \mathbf{R}_{\mathcal{b}}^{\mathcal{I}} \end{bmatrix} \bar{\mathbf{N}},$$

$$\bar{\mathbf{N}} = \begin{bmatrix} 0 & l\cos(\alpha_T) & 0 & -l\cos(\alpha_T) \\ -l\cos(\alpha_T) & 0 & l\cos(\alpha_T) & 0 \\ \frac{k_\tau}{b} & -\frac{k_\tau}{b} & \frac{k_\tau}{b} & -\frac{k_\tau}{b} \\ -\sin(\alpha_T) & 0 & \sin(\alpha_T) & 0 \\ 0 & -\sin(\alpha_T) & 0 & \sin(\alpha_T) \\ \cos(\alpha_T) & \cos(\alpha_T) & \cos(\alpha_T) & \cos(\alpha_T) \end{bmatrix},$$

where l is the distance between the propellers and the reference frame $\mathcal{F}_{\mathcal{b}}$, b is the propeller thrust coefficient, and k_τ is the propeller drag coefficient. The UAM physical parameters are given in Table 1.

Unmanned aerial manipulator parameters.

Parameter	Value
l	0.3 (m)
b	9.510^{-6} (N·s^2)
k_τ	1.710^{-7} (N·m·s^2)
α_T	5°
g	9.81 (m/s^2)
m_q	2.24 (kg)
$\mathcal{I}_q$	diag$(0.0118, 0.0235, 0.0117)$ (kg·m^2)
$m_{l_1}, m_{l_2}, m_{l_3}$	0.2 (kg)
$\mathcal{I}_{l_1}, \mathcal{I}_{l_2}, \mathcal{I}_{l_3}$	diag$(0.0011, 0.0011, 0.0012)$ (kg·m^2)

Denavit-Hartenberg parameters.

link	d_i (m)	ϑ_i (rad)	a_i (m)	α_i (rad)
l_1	0	$0.3670 + \beta_1$	0.0765	0
l_2	0	$2.5813 + \beta_2$	0.1485	0
l_3	0	$2.9486 + \beta_3$	0.1635	$\pi/2$

Table 1. Table of system parameters.

3. CONTROLLER DESIGN

This section presents the design of the nonlinear $\mathscr{H}_\infty$ and $\mathscr{W}_\infty$ controllers for the UAM. Since the UAM is underactuated, it is well known that at most n_c degrees of freedom (DOF) can be regulated at a given reference value (Siqueira and Terra, 2004a). Because of this fact, we split the vector of generalized coordinates $\mathbf{q} \in \mathbb{R}^n$ in two parts $\mathbf{q} \triangleq \left[\mathbf{q}_s'\ \mathbf{q}_c'\right]'$, in which the vector $\mathbf{q}_s \in \mathbb{R}^{n_s}$ represents the stabilized DOF and $\mathbf{q}_c \in \mathbb{R}^{n_c}$ the controlled ones.

The controllers are designed in order to achieve trajectory tracking of the controlled DOF while stabilizing the remaining ones. Regarding that the quadrotor UAV needs to change its roll and pitch angles to perform movements in the x and y directions. Thus, it is necessary to choose either these angles or the x and y positions as the controlled DOF (Raffo et al., 2011). In order to design a single layer control law, the stabilized DOF are chosen as $\mathbf{q}_s \triangleq [\phi\ \theta]'$, while the controlled DOF are chosen as $\mathbf{q}_c \triangleq [\psi\ x\ y\ z\ \beta_1\ \beta_2\ \beta_3]'$. Consequently, the system (6) is partitioned as

$$\begin{bmatrix} \mathbf{M}_{ss} & \mathbf{M}_{sc} \\ \mathbf{M}_{cs} & \mathbf{M}_{cc} \end{bmatrix} \begin{bmatrix} \ddot{\mathbf{q}}_s \\ \ddot{\mathbf{q}}_c \end{bmatrix} + \begin{bmatrix} \mathbf{C}_{ss} & \mathbf{C}_{sc} \\ \mathbf{C}_{cs} & \mathbf{C}_{cc} \end{bmatrix} \begin{bmatrix} \dot{\mathbf{q}}_s \\ \dot{\mathbf{q}}_c \end{bmatrix} + \begin{bmatrix} \mathbf{G}_s \\ \mathbf{G}_c \end{bmatrix} = \begin{bmatrix} \mathbf{B}_s \\ \mathbf{B}_c \end{bmatrix} \boldsymbol{\Gamma} + \begin{bmatrix} \boldsymbol{\delta}_s \\ \boldsymbol{\delta}_c \end{bmatrix}. \tag{10}$$

Note that the matrices $\mathbf{B}_s$ must have full row rank, and $\mathbf{B}_c$ must be invertible for all t. The following controllers are derived based on (10).

3.1 Nonlinear $\mathscr{H}_\infty$ control design

The $\mathscr{H}_\infty$ control approach used in this work is based on the controller proposed in Raffo et al. (2011). In order to design the nonlinear $\mathscr{H}_\infty$ controller, system (10) is normalized to obtain a block diagonal inertia matrix by

$$\mathbf{T}_m = \begin{bmatrix} \mathbb{1} & -\mathbf{M}_{sc}\mathbf{M}_{cc}^{-1} \\ -\mathbf{M}_{cs}\mathbf{M}_{ss}^{-1} & \mathbb{1} \end{bmatrix}, \tag{11}$$

which leads to

$$\underbrace{\begin{bmatrix} \mathbf{M}_{or} & \mathbf{0} \\ \mathbf{0} & \mathbf{M}_{ic} \end{bmatrix}}_{\overline{\mathbf{M}}(\mathbf{q})} \begin{bmatrix} \ddot{\mathbf{q}}_s \\ \ddot{\mathbf{q}}_c \end{bmatrix} + \underbrace{\begin{bmatrix} \mathbf{C}_{or} & \mathbf{C}_{oc} \\ \mathbf{C}_{ir} & \mathbf{C}_{ic} \end{bmatrix}}_{\overline{\mathbf{C}}(\mathbf{q},\dot{\mathbf{q}})} \begin{bmatrix} \dot{\mathbf{q}}_s \\ \dot{\mathbf{q}}_c \end{bmatrix} + \underbrace{\begin{bmatrix} \mathbf{G}_{or} \\ \mathbf{G}_{ic} \end{bmatrix}}_{\overline{\mathbf{G}}(\mathbf{q})} = \underbrace{\begin{bmatrix} \overline{\mathbf{\Gamma}}_{or} \\ \overline{\mathbf{\Gamma}}_{ic} \end{bmatrix}}_{\overline{\mathbf{\Gamma}}(\mathbf{q})} + \underbrace{\begin{bmatrix} \boldsymbol{\delta}_{or} \\ \boldsymbol{\delta}_{ic} \end{bmatrix}}_{\bar{\boldsymbol{\delta}}(t)}, \tag{12}$$

with $\overline{\mathbf{M}}(\mathbf{q}) = \mathbf{T}_m(\mathbf{q})\mathbf{M}$, $\overline{\mathbf{C}}(\mathbf{q},\ \dot{\mathbf{q}}) = \mathbf{T}_m(\mathbf{q})\mathbf{C}(\mathbf{q},\dot{\mathbf{q}})$, $\overline{\mathbf{G}}(\mathbf{q}) = \mathbf{T}_m(\mathbf{q})\mathbf{G}(\mathbf{q})$, $\overline{\mathbf{\Gamma}}(\mathbf{q}) = \mathbf{T}_m(\mathbf{q})\mathbf{B}(\mathbf{q})\mathbf{\Gamma}$, and $\bar{\boldsymbol{\delta}}(t) = \mathbf{T}_m(\mathbf{q})\boldsymbol{\delta}(t)$.

Afterwards, the tracking error vector is defined as

$$\mathbf{x} = \begin{bmatrix} \dot{\mathbf{q}}_s \\ \dot{\tilde{\mathbf{q}}}_c \\ \tilde{\mathbf{q}}_c \\ \displaystyle\int \tilde{\mathbf{q}}_c \mathrm{dt} \end{bmatrix} = \begin{bmatrix} \dot{\mathbf{q}}_s \\ \dot{\mathbf{q}}_c - \dot{\mathbf{q}}_{c_r} \\ \mathbf{q}_c - \mathbf{q}_{c_r} \\ \displaystyle\int \mathbf{q}_c - \mathbf{q}_{c_r} \mathrm{dt} \end{bmatrix}, \tag{13}$$

where $\mathbf{q}_{c_r}$, $\dot{\mathbf{q}}_{c_r}$, and $\dot{\mathbf{q}}_{c_r}$ are the desired values for the controlled DOF and its time derivatives. In addition, the following state transformation is defined

$$\mathbf{z} = \begin{bmatrix} \mathbf{z}_1 \\ \mathbf{z}_2 \\ \mathbf{z}_3 \\ \mathbf{z}_4 \end{bmatrix} = \mathbf{T}_0\mathbf{x} = \begin{bmatrix} \mathbf{T}_{11} & \mathbf{0} & \mathbf{0} & \mathbf{0} \\ \mathbf{0} & \mathbf{T}_{22} & \mathbf{T}_{23} & \mathbf{T}_{24} \\ \mathbf{0} & \mathbf{0} & \mathbb{1} & \mathbb{1} \\ \mathbf{0} & \mathbf{0} & \mathbf{0} & \mathbb{1} \end{bmatrix} \mathbf{x}, \tag{14}$$

where $\mathbf{T}_{11} = \rho\mathbb{1}$, $\mathbf{T}_{22} = \nu\mathbb{1}$, with $\rho, \nu \in \mathbb{R}^+$, and $\mathbf{T}_{23}$ and $\mathbf{T}_{24}$ are matrices with appropriate dimension. Despite of this transformation, the following change of variables over the control action and disturbances is also considered

$$\overline{\mathbf{M}}(\mathbf{q})\mathbf{T}\dot{\mathbf{x}} + \overline{\mathbf{C}}(\mathbf{q},\dot{\mathbf{q}})\mathbf{T}\mathbf{x} = \bar{\mathbf{u}} + \bar{\mathbf{d}}, \tag{15}$$

where $\mathbf{T} \triangleq \begin{bmatrix} \mathbf{T}_{11} & \mathbf{0} & \mathbf{0} & \mathbf{0} \\ \mathbf{0} & \mathbf{T}_{22} & \mathbf{T}_{23} & \mathbf{T}_{24} \end{bmatrix}$.

Accordingly, by expanding these transformations and written system (12) with respect to the tracking error variables, the following error dynamic state-space system is obtained

$$\dot{\mathbf{x}} = \mathbf{f}(\mathbf{x},\mathbf{q}_s,t) + \mathbf{g}(\mathbf{x},\mathbf{q}_s,t)\overline{\mathbf{u}} + \mathbf{k}(\mathbf{x},\mathbf{q}_s,t)\overline{\mathbf{d}}, \tag{16}$$

where,

$$\mathbf{f}(\mathbf{x},\mathbf{q}_s,t) \triangleq \mathbf{T}_0^{-1}\mathbf{F}\mathbf{T}_0\mathbf{x},$$

$$\mathbf{F} \triangleq \begin{bmatrix} -\mathbf{M}_{or}^{-1}\mathbf{C}_{or} & -\mathbf{M}_{or}^{-1}\mathbf{C}_{oc} & \mathbf{0} & \mathbf{0} \\ -\mathbf{M}_{ic}^{-1}\mathbf{C}_{ir} & -\mathbf{M}_{ic}^{-1}\mathbf{C}_{ic} & \mathbf{0} & \mathbf{0} \\ \mathbf{0} & \mathbf{T}_{22}^{-1} & \mathbb{1} - \mathbf{T}_{22}^{-1}\mathbf{T}_{23} & -\mathbb{1} - \mathbf{T}_{22}^{-1}(\mathbf{T}_{23} - \mathbf{T}_{24}) \\ \mathbf{0} & \mathbf{0} & \mathbb{1} & -\mathbb{1} \end{bmatrix},$$

$$\mathbf{g}(\mathbf{x},\mathbf{q}_s,t) = \mathbf{k}(\mathbf{x},\mathbf{q}_s,t) \triangleq \mathbf{T}_0^{-1} \begin{bmatrix} \mathbf{M}_{or}^{-1} & \mathbf{0} \\ \mathbf{0} & \mathbf{M}_{ic}^{-1} \\ \mathbf{0} & \mathbf{0} \\ \mathbf{0} & \mathbf{0} \end{bmatrix},$$

and the transformed control input and external disturbances vector are given by $\bar{\mathbf{u}} = \mathbf{T}_c(-\mathbf{N} + \overline{\mathbf{\Gamma}})$, and $\bar{\mathbf{d}} = \overline{\mathbf{M}}(\mathbf{q})\mathbf{T}_c\overline{\mathbf{M}}^{-1}(\mathbf{q})\bar{\boldsymbol{\delta}}$, respectively, in which $\mathbf{N} \triangleq \mathbf{M}_{cc}(\ddot{\mathbf{q}}_{c_r} - \mathbf{T}_1^{-1}\mathbf{T}_2\dot{\tilde{\mathbf{q}}}_c - \mathbf{T}_1^{-1}\mathbf{T}_3\tilde{\mathbf{q}}_c) + \mathbf{G}_c + \mathbf{C}_{cc}(\dot{\mathbf{q}}_{c_r} - \mathbf{T}_1^{-1}\mathbf{T}_2\tilde{\mathbf{q}}_c - \mathbf{T}_1^{-1}\mathbf{T}_3 \int \tilde{\mathbf{q}}_c dt)$, and $\mathbf{T}_c \triangleq \mathrm{blkdiag}(\mathbf{T}_1, \mathbf{T}_2)$, where blkdiag$(\cdot)$ stands for a block diagonal matrix.

Finally, the plant to be controlled is given by

$$\mathcal{P}_1 : \begin{cases} \dot{\mathbf{x}} = \mathbf{f}(\mathbf{x},\mathbf{q}_s,t) + \mathbf{g}(\mathbf{x},\mathbf{q}_s,t)\overline{\mathbf{u}} + \mathbf{k}(\mathbf{x},\mathbf{q}_s,t)\overline{\mathbf{d}}, \\ \boldsymbol{\zeta} = \mathbf{W} \begin{bmatrix} \mathbf{x} \\ \bar{\mathbf{u}} \end{bmatrix} \end{cases} \tag{17}$$

where $\boldsymbol{\zeta}$ is the cost variable. The classic nonlinear $\mathscr{H}_\infty$ control problem is posed as

$$V_{\mathscr{H}_\infty} = \min_{\bar{\mathbf{u}} \in \bar{\mathcal{U}}} \max_{\bar{\mathbf{d}} \in \bar{\mathcal{W}}} \frac{1}{2}\left|\boldsymbol{\zeta}\right|_{\mathcal{L}_2}^2 - \frac{1}{2}\gamma^2 \left|\bar{\mathbf{d}}\right|_{\mathcal{L}_2}^2 \tag{18}$$

where $\bar{\mathcal{U}}, \bar{\mathcal{W}} \in \mathcal{L}_2[0,\infty)$, and γ is the $\mathscr{H}_\infty$ attenuation level.

The optimization problem (18) is formulated using dynamic-programming, from which the associated Hamiltonian is given by

$$\mathbb{H}_{\mathscr{H}_\infty} = \frac{\partial V_{\mathscr{H}_\infty}}{\partial \mathbf{x}}\dot{\mathbf{x}} + \frac{\partial' V_{\mathscr{H}_\infty}}{\partial \mathbf{q}_s}\dot{\mathbf{q}}_s + \frac{1}{2}\mathbf{x}'\mathbf{Q}\mathbf{x} + \mathbf{x}'\mathbf{S}\bar{\mathbf{u}} + \frac{1}{2}\bar{\mathbf{u}}'\mathbf{R}\bar{\mathbf{u}} - \frac{1}{2}\gamma^2\bar{\mathbf{d}}'\bar{\mathbf{d}}, \tag{19}$$

with the boundary condition $V_{\mathscr{H}_\infty}(\mathbf{0}) = 0$, in which $\mathbf{Q}$, $\mathbf{S}$, and $\mathbf{R}$ are weighting matrices, and $\mathbf{W}'\mathbf{W} = \begin{bmatrix} \mathbf{Q} & \mathbf{S} \\ \mathbf{S}' & \mathbf{R} \end{bmatrix}$.

The optimal control law, $\bar{\mathbf{u}}^*$, and the worst case of disturbances, $\bar{\mathbf{d}}^*$, are computed by taking the following partial derivatives:

$$\frac{\partial \mathbb{H}_{\mathscr{H}_\infty}}{\partial \bar{\mathbf{u}}} = \mathbf{T}_m\mathbf{g}'(\mathbf{x},\mathbf{q}_s,t)\frac{\partial V_{\mathscr{H}_\infty}}{\partial \mathbf{x}} + \mathbf{S}'\mathbf{x} + \mathbf{R}\bar{\mathbf{u}} = 0, \tag{20}$$

$$\frac{\partial \mathbb{H}_{\mathscr{H}_\infty}}{\partial \bar{\mathbf{d}}} = \mathbf{T}_m\mathbf{k}'(\mathbf{x},\mathbf{q}_s,t)\frac{\partial V_{\mathscr{H}_\infty}}{\partial \mathbf{x}} - \gamma^2\bar{\mathbf{d}} = 0. \tag{21}$$

After some algebraic manipulations, the above derivatives lead to

$$\bar{\mathbf{u}}^* = -\mathbf{R}^{-1}\left(\mathbf{T}_m'\mathbf{g}(\mathbf{x},\mathbf{q}_s,t)\frac{\partial V_{\mathscr{H}_\infty}}{\partial \mathbf{x}} + \mathbf{S}'\mathbf{x}\right), \tag{22}$$

$$\bar{\mathbf{d}}^* = \frac{1}{\gamma^2}\mathbf{T}_m\mathbf{k}'(\mathbf{x},\mathbf{q}_s,t)\frac{\partial V_{\mathscr{H}_\infty}}{\partial \mathbf{x}}. \tag{23}$$

The HJ equation associated with this optimization problem is obtained by replacing the optimal control law (22) and the worst case of the disturbances (23) in (19), resulting in

$$\frac{\partial V_{\mathscr{H}_\infty}(\mathbf{x},t)}{\partial t} + \mathbb{H}_{\mathscr{H}_\infty}(V_{\mathscr{H}_\infty}(\mathbf{x},t),\mathbf{x},\mathbf{q}_s,\bar{\mathbf{u}}^*,\bar{\mathbf{d}}^*,t) = 0. \tag{24}$$

A particular solution to the HJ PDE (24) is given in Theorem 1 of Raffo et al. (2011) [3] . From the results of this theorem, the following optimal control law is obtained

$$\bar{\mathbf{u}}^* = -\mathbf{T}_m\mathbf{R}^{-1}(\mathbf{S}' + \mathbf{T})\mathbf{x}. \tag{25}$$

By replacing the optimal control law (25) into (15), assuming $\bar{\mathbf{d}} = 0$ and after some manipulations, the following transformed generalized force vector is obtained as

$$\overline{\mathbf{\Gamma}} = \overline{\mathbf{M}}(\mathbf{q})\ddot{\mathbf{q}} + \overline{\mathbf{C}}(\mathbf{q},\dot{\mathbf{q}})\dot{\mathbf{q}} + \overline{\mathbf{G}}(\mathbf{q}), \tag{26}$$

with

$$\ddot{\mathbf{q}} = \begin{bmatrix} \mathbf{0} \\ \ddot{\mathbf{q}}_{c_r} \end{bmatrix} - \mathbf{K}_D \begin{bmatrix} \mathbf{q}_s \\ \dot{\tilde{\mathbf{q}}}_c \end{bmatrix} - \mathbf{K}_P \begin{bmatrix} \mathbf{0} \\ \tilde{\mathbf{q}}_c \end{bmatrix} - \mathbf{K}_I \begin{bmatrix} \mathbf{0} \\ \int \tilde{\mathbf{q}}_c dt \end{bmatrix}. \tag{27}$$

The matrices $\mathbf{K}_D$, $\mathbf{K}_P$, and $\mathbf{K}_I$ are given in Appendix A. Consequently, the applied control input to the system (10) is given by

$$\mathbf{\Gamma} = \mathbf{B}(\mathbf{q})^{\#}\mathbf{T}_m{}^{-1}(\mathbf{q})\overline{\mathbf{\Gamma}} \tag{28}$$

[3] For more details about the proof of this theorem see Raffo et al. (2011) and for the stability proof of the proposed $\mathscr{H}_\infty$ controller see Raffo et al. (2015)

where $(\cdot)^{\#}$ denotes the pseudo-inverse.[4]

3.2 Nonlinear $\mathscr{W}_\infty$ control design

The $\mathscr{W}_\infty$ controller formulation presented in this section is based on the formulation introduced by Neri et al. (2018). The first step to design this controller is to rewrite system (10) as the following tracking error dynamics

$$\mathbf{M}(\mathbf{q}_s,\tilde{\mathbf{q}}_c+\mathbf{q}_{c_r})\begin{bmatrix}\ddot{\mathbf{q}}_s\\ \ddot{\tilde{\mathbf{q}}}_c+\ddot{\mathbf{q}}_{c_r}\end{bmatrix}+\mathbf{C}(\mathbf{q}_s,\tilde{\mathbf{q}}_c+\mathbf{q}_{c_r},\dot{\mathbf{q}}_s,\dot{\tilde{\mathbf{q}}}_c+\dot{\mathbf{q}}_{c_r})\begin{bmatrix}\dot{\mathbf{q}}_s\\ \dot{\tilde{\mathbf{q}}}_c+\dot{\mathbf{q}}_{c_r}\end{bmatrix}$$
$$+\mathbf{G}(\mathbf{q}_s,\tilde{\mathbf{q}}_c+\mathbf{q}_{c_r})=\mathbf{B}(\mathbf{q}_s,\tilde{\mathbf{q}}_c+\mathbf{q}_{c_r})\boldsymbol{\Gamma}+\boldsymbol{\delta}(t), \quad (29)$$

where $\tilde{\mathbf{q}}_c$ and $\mathbf{q}_{c_r}$ are defined as in (13).

Then, the following change of variables over the control inputs is considered in (29),

$$\mathbf{u}=\mathbf{B}(\mathbf{q}_s,\tilde{\mathbf{q}}_c+\mathbf{q}_{c_r})\boldsymbol{\Gamma}-\mathbf{G}(\mathbf{q}_s,\tilde{\mathbf{q}}_c+\mathbf{q}_{c_r})-\mathbf{M}(\mathbf{q}_s,\tilde{\mathbf{q}}_c+\mathbf{q}_{c_r})\begin{bmatrix}\mathbf{0}\\ \ddot{\mathbf{q}}_{c_r}\end{bmatrix}$$
$$-\mathbf{C}(\mathbf{q}_s,\tilde{\mathbf{q}}_c+\mathbf{q}_{c_r},\dot{\mathbf{q}}_s,\dot{\tilde{\mathbf{q}}}_c+\dot{\mathbf{q}}_{c_r})\begin{bmatrix}\mathbf{0}\\ \dot{\mathbf{q}}_{c_r}\end{bmatrix}. \quad (30)$$

The main idea is to include in the optimization problem only forces and torques that affect the kinetic energy of the system. Considering (30), equation (29) result in

$$\mathbf{M}(\mathbf{q}_s,\tilde{\mathbf{q}}_c+\mathbf{q}_{c_r})\begin{bmatrix}\ddot{\mathbf{q}}_s\\ \ddot{\tilde{\mathbf{q}}}_c\end{bmatrix}+\mathbf{C}(\mathbf{q}_s,\tilde{\mathbf{q}}_c+\mathbf{q}_{c_r},\dot{\mathbf{q}}_s,\dot{\tilde{\mathbf{q}}}_c+\dot{\mathbf{q}}_{c_r})\begin{bmatrix}\dot{\mathbf{q}}_s\\ \dot{\mathbf{q}}_{c_r}\end{bmatrix}=\mathbf{u}+\boldsymbol{\delta}, \quad (31)$$

which is similar to the transformation (15) used in the nonlinear $\mathscr{H}_\infty$ control design, but without the need to normalize the system.

In addition, considering the state vector defined in (13), equation (31) is expressed in the state-space as

$$\dot{\mathbf{x}}=\underbrace{\begin{bmatrix}\mathbf{M}^{-1}\mathbf{C} & \mathbf{0} & \mathbf{0}\\ \begin{bmatrix}\mathbf{0} & \mathbb{1}\end{bmatrix} & \mathbf{0} & \mathbf{0}\\ \mathbf{0} & \mathbb{1} & \mathbf{0}\end{bmatrix}}_{\mathbf{f}(\mathbf{x},\mathbf{q}_s)}\mathbf{x}+\underbrace{\begin{bmatrix}\mathbf{M}^{-1}\\ \mathbf{0}\\ \mathbf{0}\end{bmatrix}}_{\mathbf{g}(\mathbf{x},\mathbf{q}_s)}\mathbf{u}+\underbrace{\begin{bmatrix}\mathbf{M}^{-1}\\ \mathbf{0}\\ \mathbf{0}\end{bmatrix}}_{\mathbf{k}(\mathbf{x},\mathbf{q}_s)}\boldsymbol{\delta}. \quad (32)$$

Then, the plant to be controlled is given by

$$\mathcal{P}_2:\begin{cases}\dot{\mathbf{x}} &= \mathbf{f}(\mathbf{x},\mathbf{q}_s)+\mathbf{g}(\mathbf{x},\mathbf{q}_s)\mathbf{u}+\mathbf{k}(\mathbf{x},\mathbf{q}_s)\boldsymbol{\delta},\\ \mathbf{z}_c &= \int_0^t \tilde{\mathbf{q}}_c(t)dt,\\ \mathbf{z}_s &= \dot{\tilde{\mathbf{q}}}_s(t),\end{cases} \quad (33)$$

where $\mathbf{z}_c$ and $\mathbf{z}_s$ are the cost variables associated with the controlled and stabilized DOF, respectively.

The nonlinear $\mathscr{W}_\infty$ control problem is then posed as[5]

$$V_{\mathscr{W}_\infty}=\min_{\mathbf{u}\in\mathcal{U}}\max_{\boldsymbol{\delta}\in\mathcal{W}}\frac{1}{2}\left\|\mathbf{z}_c\right\|^2_{\mathscr{W}_{3,2,\boldsymbol{\Lambda}}}+\frac{1}{2}\left\|\mathbf{z}_s\right\|^2_{\mathscr{W}_{1,2,\boldsymbol{\Upsilon}}}-\frac{1}{2}\gamma^2\|\boldsymbol{\delta}\|^2_{\mathcal{L}_2} \quad (34)$$

where $\mathcal{U}\subseteq\mathbb{R}^c$, $\mathcal{W}\in\mathcal{L}_2[0,\infty)$, and $\boldsymbol{\Lambda}=\{\boldsymbol{\Lambda}_0,\ \boldsymbol{\Lambda}_1,\ \boldsymbol{\Lambda}_2,\ \boldsymbol{\Lambda}_3\}$ and $\boldsymbol{\Upsilon}=\{\boldsymbol{\Upsilon}_0,\ \boldsymbol{\Upsilon}_1\}$ are composed of symmetric and positive definite tuning matrices, that weight the influence of the states in the control objective, and γ is the $\mathcal{W}_\infty$ attenuation level.

The optimization problem (34) is formulated using dynamic-programming, from which the associated Hamiltonian is given by

$$\mathbb{H}_{\mathscr{W}_\infty}(V_{\mathscr{W}_\infty},\mathbf{x},\mathbf{q}_s,\mathbf{u},t)=\frac{\partial' V_{\mathscr{W}_\infty}}{\partial\mathbf{x}}\dot{\mathbf{x}}+\frac{1}{2}\mathbf{z}'_c\boldsymbol{\Lambda}_0\mathbf{z}_c+\frac{1}{2}\dot{\mathbf{z}}'_c\boldsymbol{\Lambda}_1\dot{\mathbf{z}}_c$$
$$+\frac{1}{2}\ddot{\mathbf{z}}_c\boldsymbol{\Lambda}_2\ddot{\mathbf{z}}_c+\frac{1}{2}\dddot{\mathbf{z}}'_c\boldsymbol{\Lambda}_3\dddot{\mathbf{z}}_c+\frac{1}{2}\mathbf{z}'_s\boldsymbol{\Upsilon}_0\mathbf{z}_s+\frac{1}{2}\dot{\mathbf{z}}'_s\boldsymbol{\Upsilon}_1\dot{\mathbf{z}}_s-\frac{1}{2}\gamma^2\boldsymbol{\delta}'\boldsymbol{\delta}. \quad (35)$$

with the boundary condition $V_{\mathscr{W}_\infty}(\mathbf{0})=0$.

The optimal control law and the worst case of disturbances are computed by taking the partial derivatives of (35) as follows

$$\frac{\partial\mathbb{H}_{\mathscr{W}_\infty}}{\partial\mathbf{u}}=\mathbf{g}'\frac{\partial V_{\mathscr{W}_\infty}}{\partial\mathbf{x}}-\boldsymbol{\Pi}\mathbf{C}\dot{\tilde{\mathbf{q}}}+\boldsymbol{\Pi}\boldsymbol{\delta}^*+\boldsymbol{\Pi}\mathbf{u}^*=0, \quad (36)$$
$$\frac{\partial\mathbb{H}_{\mathscr{W}_\infty}}{\partial\boldsymbol{\delta}}=\mathbf{k}'\frac{\partial V_{\mathscr{W}_\infty}}{\partial\mathbf{x}}-\boldsymbol{\Pi}\mathbf{C}\dot{\tilde{\mathbf{q}}}+\boldsymbol{\Pi}\boldsymbol{\delta}^*+\boldsymbol{\Pi}\mathbf{u}^*-\gamma^2\boldsymbol{\delta}^*=0, \quad (37)$$

where $\boldsymbol{\Pi}\triangleq\mathbf{M}^{-1}\mathbf{E}\mathbf{M}^{-1}$ with $\mathbf{E}\triangleq\operatorname{blkdiag}(\boldsymbol{\Upsilon}_1,\boldsymbol{\Lambda}_3)$. According, the optimal control law is obtained from (36), with some algebraic manipulations, and is given by

$$\mathbf{u}^*=-\boldsymbol{\Pi}\mathbf{g}'\frac{\partial V_{\mathscr{W}_\infty}}{\partial\mathbf{x}}+\mathbf{C}\tilde{\mathbf{q}}-\boldsymbol{\delta}^*. \quad (38)$$

In addition, the worst case of the disturbances is computed by subtracting (37) from (36), yielding

$$\boldsymbol{\delta}^*=\frac{1}{\gamma^2}\left(\mathbf{k}'-\mathbf{g}'\right)\frac{\partial V_{\mathscr{W}_\infty}}{\partial\mathbf{x}}. \quad (39)$$

The HJ equation associated with the optimization problem is obtained by replacing the optimal control law and the worst case of the disturbances in (35), which results in

$$\frac{\partial V_{\mathscr{W}_\infty}(\mathbf{x},t)}{\partial t}+\mathbb{H}_{\mathscr{W}_\infty}(V_{\mathscr{W}_\infty}(\mathbf{x},t),\mathbf{x},\mathbf{q}_s,\mathbf{u}^*,\boldsymbol{\delta}^*,t)=0. \quad (40)$$

A particular solution to the HJ PDE (40) is given in Theorem 1 of Neri et al. (2018). From the results of this Theorem, the optimal control law (38) and system (29), assuming $\boldsymbol{\delta}=0$, the applied control input is given by

$$\boldsymbol{\Gamma}=\mathbf{B}^{\#}(\mathbf{q}_s,\tilde{\mathbf{q}}_c+\mathbf{q}_{c_r})\left(\mathbf{G}+\mathbf{M}\begin{bmatrix}\mathbf{0}\\ \ddot{\mathbf{q}}_{c_r}\end{bmatrix}+\mathbf{C}\dot{\mathbf{q}}\right.$$
$$\left.-\mathbf{M}\begin{bmatrix}\boldsymbol{\Upsilon}_1^{-1}\mathbf{U} & \mathbf{0} & \mathbf{0} & \mathbf{0}\\ \mathbf{0} & \boldsymbol{\Lambda}_3^{-1}\mathbf{Q} & \boldsymbol{\Lambda}_3^{-1}\mathbf{K} & \boldsymbol{\Lambda}_3^{-1}\mathbf{F}\end{bmatrix}\mathbf{x}\right), \quad (41)$$

with $\mathbf{U}=\sqrt{\boldsymbol{\Upsilon}_0}\sqrt{\boldsymbol{\Upsilon}_1}$, $\mathbf{F}=\sqrt{\boldsymbol{\Lambda}_0}\sqrt{\boldsymbol{\Lambda}_3}$, and $\mathbf{Q}$ and $\mathbf{K}$ given by the solution of the following pair of Riccati equations

$$-\mathbf{K}\boldsymbol{\Lambda}_3^{-1}\mathbf{K}+2\mathbf{Q}\sqrt{\boldsymbol{\Lambda}_0}\sqrt{\boldsymbol{\Lambda}_3}+\boldsymbol{\Lambda}_1=\mathbf{0}, \quad (42)$$
$$-\mathbf{Q}\boldsymbol{\Lambda}_3^{-1}\mathbf{Q}+2\mathbf{K}+\boldsymbol{\Lambda}_2=\mathbf{0}. \quad (43)$$

4. NUMERICAL EXPERIMENTS

This section presents the results of numerical experiments in order to evaluate the performance and compare the nonlinear $\mathscr{H}_\infty$ and $\mathscr{W}_\infty$ controllers.

The experiments were conducted using the high fidelity ProVANT simulator (Lara et al., 2018) in a HIL framework (see Figure 5). The UAM was simulated in a computer equipped with an Intel Core i7-7500U dual-core processor running at 2.9 GHz, 16 GB of RAM and an NVidia 920MX GPU with Ubuntu Linux version 18.04, while the controllers were executed in an embedded system consisting

[4] It is assumed that the controller is robust enough to handle errors generated by the use of the pseudo-inverse.

[5] The weighted Sobolev $\mathcal{W}_{m,p,\boldsymbol{\sigma}}-$norm of a function $\mathbf{z}(t):\mathbb{R}^+\to\mathbb{R}$, for $m\in\mathbb{N}$ and $p\in\mathbb{N}\cup\{\infty\}$, is defined as $||\mathbf{z}(t)||_{\mathcal{W}_{m,p,\boldsymbol{\sigma}}}=\Big(\sum_{\alpha=0}^{m}||\frac{d^\alpha\mathbf{z}(t)}{dt^\alpha}||^p_{\mathcal{L}_p,\boldsymbol{\sigma}_\alpha}\Big)^{1/p}$, where $\boldsymbol{\sigma}=\{\boldsymbol{\sigma}_0,...,\boldsymbol{\sigma}_m\}$, in which $\boldsymbol{\sigma}_\alpha$ is a symmetric and positive definite weighting matrix with appropriate dimension, and $||\cdot||_{\mathcal{L}_p,\boldsymbol{\sigma}_\alpha}$ stands for the $\mathcal{L}_p-$ norm weighted by the matrix $\boldsymbol{\sigma}_\alpha$.

of a STM32 Discovery development kit equipped with an STM32F407VGT6 with 1 MB of Flash storage and 192 KB of RAM. The computer and the embedded system communicate using a virtual serial port running at 115200bps baud rate through a USB connection. This embedded system will be later part of the physical prototype. The aim is to validate the control laws before performing real flight experiments.

During the numerical experiments, the UAM performs a mission composed of the following stretches: (i) the UAM starts displaced from the desired trajectory at position $x = 0.5$, $y = 2.7$, $z = 0$, and with the remaining states equal to zero; (ii) the UAM goes through an intermediate point in the position $x = y = 1.5$, and $z = 1$; (iii) the UAM goes to the target position $x = 2.5$, $y = 2.7$, $z = 1$ and hovers while extending its manipulator arm; (iv) the UAM retracts the manipulator arm; (v) the UAM returns to the starting position and lands.

Considering these waypoints, a RRT path planner (Choset; et al., 2005) was implemented in order to generate the reference trajectory to be used by the controllers. The aim is to evaluate the following features: the performance of the UAM operating in hovering mode; the ability of tracking a time-varying trajectory with small enough error; the behavior of the system under movements of the robotic arm; the ability of operating when affected by bounded external disturbances.

The $\mathscr{H}_\infty$ controller was implemented taking into account the control law (28) and was tuned with $\omega_{us} = 0.55$, $\omega_{uc} = 8.45$, $\omega_{1s} = 3.2$, $\omega_{1c} = 0.55$, $\omega_{2c} = 0.75$, $\omega_{3c} = 2.75$. The $\mathscr{W}_\infty$ controller was implemented taking into account (41) and was tuned with $\boldsymbol{\Upsilon}_0 = \text{diag}(50, 50)$, $\boldsymbol{\Upsilon}_1 = \mathbb{1}_{2\times 2}$, $\boldsymbol{\Lambda}_0 = \text{diag}(0.35, 0.001, 0.001, 0.001, 0.05, 0.08, 0.08)$, $\boldsymbol{\Lambda}_1 = \text{diag}(1, 1, 1, 1, 0.1, 0.1, 0.1)$, $\boldsymbol{\Lambda}_2 = \text{diag}(0.1, 0.01, 0.01, 1, 0.1, 0.1, 0.1)$, $\boldsymbol{\Lambda}_3 = \text{diag}(0.01, 0.01, 0.01, 0.1, 0.01, 0.01, 0.01)$, where $\text{diag}(\cdot)$ stands for a diagonal matrix.

During the numerical experiments, the following external disturbances (see (6)) are applied to the system starting at 82.5 seconds: $\delta_z = 1.8$ $[N]$, $\delta_x = \delta_y = 0.1$ $[N]$, $\delta_\phi = \delta_\theta = \delta_\psi = \delta_{\beta_1} = \delta_{\beta_2} = \delta_{\beta_3} = 0.02$ $[N \cdot m]$. These disturbances can be seen as the effects generated by the pick-up and transportation of an object with approximately 200g of mass. Additionally, disturbances $\delta_z = 3$ $[N]$ and $\delta_y = 1$ $[N]$, that affect the whole system due to the dynamical coupling, were applied in the interval between 40 and 60 seconds. The results are shown [6] in Figures 2 and 3.

At the beginning of the experiments, the UAM starts vertically displaced from the desired trajectory and converges to it after only few seconds. After 60 seconds of simulation, the UAM extends its manipulator arm. Despite the existence of small oscillations, it remains stable while executing the maneuver. Besides, the effects of the external disturbances are attenuated by both control strategies.

It is also verified that the $\mathscr{W}_\infty$ controller provides less oscillatory closed-loop behavior. This happens thanks to the fact that the time derivatives of the cost variable are considered in the cost functional of the $\mathscr{W}_\infty$ control

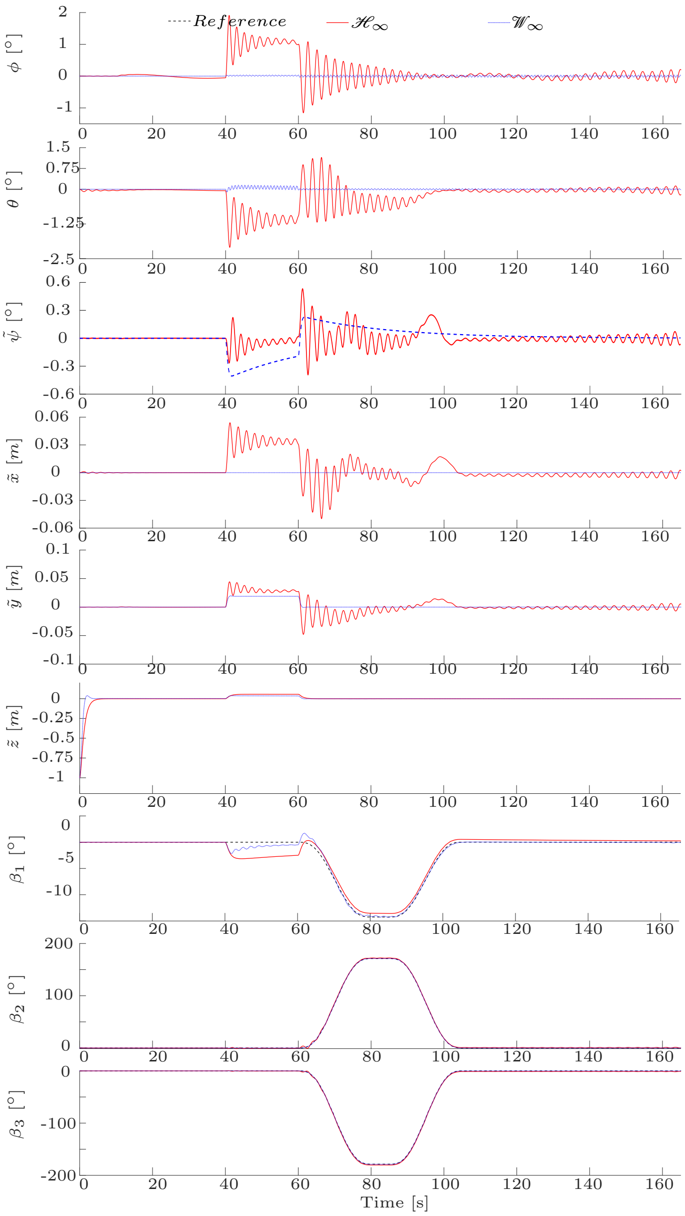

Figure 2. Roll and pitch angles, error of translational position and yaw angle, and angles of the manipulator arm.

formulation (see eq. (34)). In addition, the system is more responsive to the effects of external disturbances. Moreover, as can be seen in Appendix A, in the formulation of the nonlinear $\mathscr{H}_\infty$ controller presented in Section 3, the weighting matrices must be considered as positive real scalars multiplied by the identity matrix, preventing the appropriate tuning of the control law parameters for the UAM.

It is also verified that the $\mathscr{W}_\infty$ controller reacts faster when the system is subjected to external disturbances and converges faster to the equilibrium point. In addition, it achieves better performance with respect to the ISE index even with smaller control efforts, which is verified through the IADU index, as shown in Table 2.

Furthermore, as the system has at least three very different dynamics (the quadrotor UAV positions, the quadrotor UAV attitude, and the robotic manipulator angular po-

[6] A video recording of the experiments is available in `https://youtu.be/3SSt-10IXu4`.

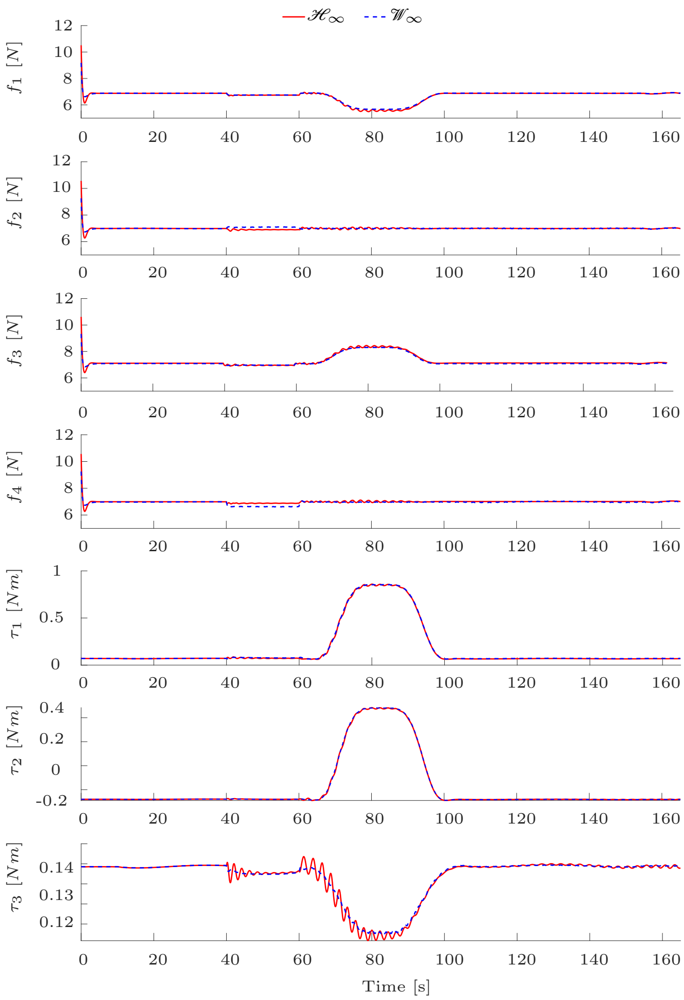

Figure 3. Applied control inputs.

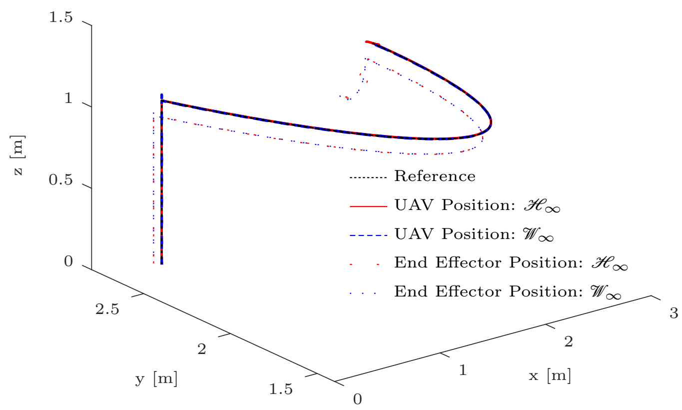

Figure 4. 3D trajectory of the UAV and end effector.

sitions), the smaller number of tuning DOF of the $\mathscr{H}_\infty$ controller imposes limitations in the syntonization of the controller and consequently in performance. As the $\mathscr{W}_\infty$ control strategy allows the separate weighting of each DOF, it is possible to achieve a better closed-loop response, a clear advantage over the $\mathscr{H}_\infty$ control formulation considering only the separation of the system in stabilized and controlled dynamics.

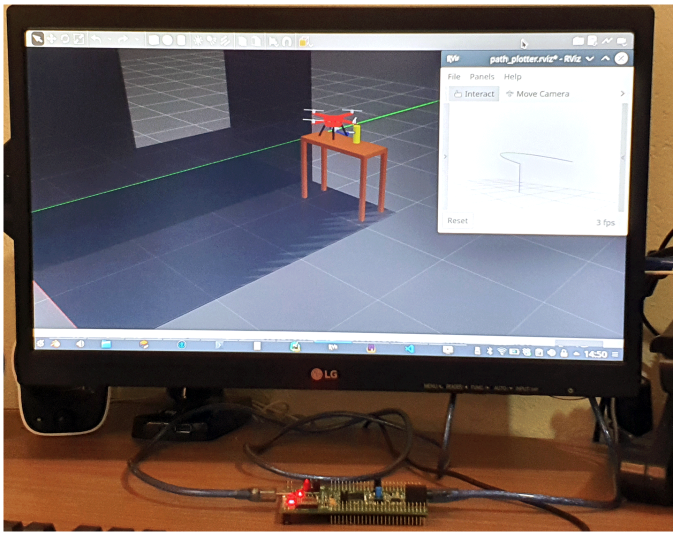

Figure 5. Experimental setup of the HIL simulation.

P. index	Definition	$\mathscr{W}_\infty$	$\mathscr{H}_\infty$	$\mathscr{H}_\infty$ / $\mathscr{W}_\infty$
IADU	$\int_0^T \sum_{i=1}^{7} \left\lvert \frac{d\Gamma_i}{dt} \right\rvert dt$	**355740**	461702	129,79%
ISE	$\int_0^T (\psi - \psi_r)^2\, dt$	**2,0147**	13,3548	662,87%
	$\int_0^T (x - x_r)^2\, dt$	**6,0066**	127,3446	2120,08%
	$\int_0^T (y - y_r)^2\, dt$	**38,3762**	118,0508	307,62%
	$\int_0^T (z - z_r)^2\, dt$	**158,8396**	240,94	151,69%
	$\int_0^T (\beta_1 - \beta_{1_r})^2\, dt$	**65,3935**	178,0235	272,23%
	$\int_0^T (\beta_2 - \beta_{2_r})^2\, dt$	**8,7688**	72,6795	828,84%
	$\int_0^T (\beta_3 - \beta_{3_r})^2\, dt$	**3,8775**	41,8346	1078,91%

Table 2. Performance indexes table.

5. CONCLUSION

This work presented the dynamic modeling of a UAM and the design of nonlinear $\mathscr{H}_\infty$ and $\mathscr{W}_\infty$ controllers for a robust trajectory tracking. These controllers were implemented using the ProVANT simulator in a HIL framework. A comparative analysis has been conducted, which showed that the nonlinear $\mathscr{W}_\infty$ controller provided better transient performance with faster reaction against external disturbances. In addition, the $\mathscr{W}_\infty$ controller achieved better results when evaluating the ISE and IADU indexes.

Moreover, in contrast to the nonlinear $\mathscr{W}_\infty$ controller, the $\mathscr{H}_\infty$ control strategy requires that weighting parameters be the same for all stabilized DOF and for all the controlled DOF (see Appendix A). Therefore, future works will include the reformulation of the nonlinear $\mathscr{H}_\infty$ control strategy to allow the individual weighting of each state variable of the system, another proposition to address this issue is the normalization of the system in terms of the time constant. In addition, since we are dealing with aerial manipulator, it is intended to reformulate these controllers taken into account constraints to limit its workspace. Finally, it is also intended to perform real flight experiments.

Appendix A. $\mathscr{H}_\infty$ CONTROL MATRICES

As in Raffo et al. (2011), the matrices $\mathbf{K}_D$, $\mathbf{K}_P$ and $\mathbf{K}_I$ in (27) are given by

$$\mathbf{K}_D = \begin{bmatrix} \mathbf{K}_{D_{ss}} & \mathbf{K}_{D_{sc}} \\ \mathbf{K}_{D_{cs}} & \mathbf{K}_{D_{cc}} \end{bmatrix}, \quad \mathbf{K}_P = \begin{bmatrix} \mathbf{0} & \mathbf{K}_{P_{sc}} \\ \mathbf{0} & \mathbf{K}_{P_{cc}} \end{bmatrix}, \quad \mathbf{K}_I = \begin{bmatrix} \mathbf{0} & \mathbf{K}_{I_{sc}} \\ \mathbf{0} & \mathbf{K}_{I_{cc}} \end{bmatrix},$$

where

$$\mathbf{K}_{D_{ss}} = \mathbf{M}_{or}^{-1}\left(\mathbf{C}_{or} + \frac{1}{\omega_{us}^2}\mathbb{1}\right),$$

$$\mathbf{K}_{D_{sc}} = \mathbf{M}_{or}^{-1}\left(\mathbf{C}_{oc} - \mathbf{M}_{sc}\mathbf{M}_{cc}^{-1}\frac{1}{\omega_{uc}^2}\right)\frac{\omega_{uc}\omega_{1c}}{\sqrt{\gamma^2-\omega_{uc}^2}}\frac{\sqrt{\gamma^2-\omega_{us}^2}}{\omega_{us}\omega_{1s}},$$

$$\mathbf{K}_{P_{sc}} = \mathbf{M}_{or}^{-1}\left(\mathbf{C}_{oc} - \mathbf{M}_{sc}\mathbf{M}_{cc}^{-1}\frac{1}{\omega_{uc}^2}\right)\frac{\omega_{uc}\sqrt{\omega_{2c}^2+2\omega_{1c}\omega_{3c}}}{\sqrt{\gamma^2-\omega_{uc}^2}}\frac{\sqrt{\gamma^2-\omega_{us}^2}}{\omega_{us}\omega_{1s}},$$

$$\mathbf{K}_{I_{sc}} = \mathbf{M}_{or}^{-1}\left(\mathbf{C}_{oc} - \mathbf{M}_{sc}\mathbf{M}_{cc}^{-1}\frac{1}{\omega_{uc}^2}\right)\frac{\omega_{uc}\omega_{3c}}{\sqrt{\gamma^2-\omega_{uc}^2}}\frac{\sqrt{\gamma^2-\omega_{us}^2}}{\omega_{us}\omega_{1s}},$$

$$\mathbf{K}_{D_{cs}} = \mathbf{M}_{ic}^{-1}\left(\mathbf{C}_{ir} - \mathbf{M}_{cs}\mathbf{M}_{ss}^{-1}\frac{1}{\omega_{us}^2}\right)\frac{\omega_{us}\omega_{1s}}{\sqrt{\gamma^2-\omega_{us}^2}}\frac{\sqrt{\gamma^2-\omega_{uc}^2}}{\omega_{uc}\omega_{1c}},$$

$$\mathbf{K}_{D_{cc}} = \frac{\sqrt{\omega_{2c}^2+2\omega_{1c}\omega_{3c}}}{\omega_{1s}}\mathbb{1} + \mathbf{M}_{ic}^{-1}\left(\mathbf{C}_{ic} + \frac{1}{\omega_{uc}^2}\mathbb{1}\right),$$

$$\mathbf{K}_{P_{cc}} = \frac{\sqrt{\omega_{2c}^2+2\omega_{1c}\omega_{3c}}}{\omega_{1s}}\mathbf{M}_{ic}^{-1}\left(\mathbf{C}_{ic} + \frac{1}{\omega_{uc}^2}\mathbb{1}\right) + \frac{\omega_{3c}}{\omega_{1s}}\mathbb{1},$$

$$\mathbf{K}_{I_{cc}} = \mathbf{M}_{ic}^{-1}\left(\mathbf{C}_{ic} + \frac{1}{\omega_{uc}^2}\mathbb{1}\right)\frac{\omega_{3c}}{\omega_{1s}},$$

in which it is considered the particular case where $\mathbf{Q} = \text{blkdiag}(\omega_{1s}^2\mathbb{1}, \omega_{1c}^2\mathbb{1}, \omega_{2c}^2\mathbb{1}, \omega_{3c}^2\mathbb{1})$, $\mathbf{R} = \text{blkdiag}(\omega_{ur}^2\mathbb{1}, \omega_{uc}^2\mathbb{1})$, and $\mathbf{S} = \mathbf{0}$.

REFERENCES

Acosta, J., de Cos, C.R., and Ollero, A. (2020). Accurate control of Aerial Manipulators outdoors. A reliable and self-coordinated nonlinear approach. *Aerospace Science and Technology*, 99, 105731.

Acosta, J.A., Sanchez, M.I., and Ollero, A. (2014). Robust control of underactuated Aerial Manipulators via IDA-PBC. In *IEEE Conference on Decision and Control*, 673–678. IEEE.

Aliyu, M.D.S. and Boukas, E.K. (2011). Extending nonlinear $\mathscr{H}_2$, $\mathscr{H}_\infty$ optimisation to $\mathscr{W}_{1,2}$, $\mathscr{W}_{1,\infty}$ spaces-part i: Optimal control. *Intern. J. Syst. Sci.*, 42(5), 889906.

Ballesteros-Escamilla, M.F., Cruz-Ortiz, D., Chairez, I., and Luviano-Juárez, A. (2019). Adaptive output control of a mobile manipulator hanging from a quadcopter unmanned vehicle. *ISA Transactions*, 94, 200–217.

Chilali, M. and Gahinet, P. (1996). $\mathscr{H}_\infty$ design with pole placement constraints: an LMI approach. *IEEE Transactions on automatic control*, 41(3), 358–367.

Choset;, H., Lynch, K., Hutchinson, S., Kantor, G., Burgard, W., Kavraki, L., and Thrun, S. (2005). *Principles of Robot Motion: Theory, Algorithms, and Implementations.* MIT Press, Cambridge.

Heredia, G., Jimenez-Cano, A.E., Sanchez, I., Llorente, D., Vega, V., Braga, J., Acosta, J.A., and Ollero, A. (2014). Control of a multirotor outdoor aerial manipulator. In *IEEE International Conference on Intelligent Robots and Systems*, 3417–3422. IEEE.

Jimenez-Cano, A.E., Martin, J., Heredia, G., Ollero, A., and Cano, R. (2013). Control of an aerial robot with multi-link arm for assembly tasks. In *IEEE International Conference on Robotics and Automation*, 4916–4921. IEEE.

Johansen, T.A., Andersen, T.S., and Kristiansen, R. (2019). PD+ based trajectory tracking of the underactuated quadrotor platform using dual quaternions. In *Proceedings of the American Control Conference*, volume 2019-July, 1342–1348. American Automatic Control Council.

Lara, A.V., Nascimento, I.B.P., Arias-Garcia, J., Becker, L.B., and Raffo, G.V. (2018). Hardware in The Loop Simulation Environment for Testing of Tilt-Rotor UAVs Control Strategies. In *Congresso Brasileiro de Automática - CBA*, 1–7. Sociedade Brasileira de Automática.

Lippiello, V. and Ruggiero, F. (2012). Cartesian impedance control of a uav with a robotic arm. In *IFAC Symposium on Robot Control*, 704–709. IFAC.

Mello, L.S., Raffo, G.V., and Adorno, B.V. (2015). Whole-body modeling and control of an unmanned aerial manipulator. In *XII Simpósio Brasileiro de Automação Inteligente (SBAI)*, 1–6. Sociedade Brasileira de Automática.

Nava, G., Sablé, Q., Tognon, M., Pucci, D., and Franchi, A. (2020). Direct Force Feedback Control and Online Multi-Task Optimization for Aerial Manipulators. *IEEE Robotics and Automation Letters*, 5(2), 331–338.

Neri, D., Esteban, S., and Raffo, G.V. (2018). Nonlinear $\mathscr{H}_2$ and $\mathscr{H}_\infty$ control formulated in the weighted sobolev space for underactuated mechanical systems with input coupling. In *2018 IEEE Conference on Decision and Control (CDC)*, 3812–3817. IEEE.

Raffo, G.V., Ortega, M.G., Madero, V., and Rubio, F.R. (2015). Two-wheeled self-balanced pendulum workspace improvement via underactuated robust nonlinear control. *Control Engineering Practice*, 44, 231–242.

Raffo, G.V., Ortega, M.G., and Rubio, F.R. (2011). Nonlinear $\mathscr{H}_\infty$ controller for the quad-rotor helicopter with input coupling. *IFAC Proceedings Volumes*, 44(1), 13834 – 13839.

Siqueira, A.A. and Terra, M.H. (2004a). Nonlinear $\mathscr{H}_\infty$ control for underactuated manipulators with robustness tests. *Revista Controle & Automação*, 15(3), 339–350.

Siqueira, A.A.G. and Terra, M.H. (2004b). Nonlinear and Markovian $\mathscr{H}_\infty$ controls of underactuated manipulators. *IEEE Transactions on Control Systems Technology*, 12(6), 811–826.

Spong, M.W., Hutchinson, S., and Vidyasagar, M. (2006). *Robot Modeling and Control.* Jhon Wiley & Sons, inc.

van der Schaft, A. (2000). *L2-Gain and Passivity Techniques in Nonlinear Control.* Springer Verlag, London, 2 edition.